Iranian Journal of Electrical and Electronic Engineering No. (2026) pp-pp

Iran University of Science and Technology

Iranian Journal of Electrical and Electronic Engineering

Journal Homepage: ijeee.iust.ac.ir

A Modified Hybrid PM-Reluctance Coaxial Magnetic Gear with an Alternate Rotor

Mostafa Madanchi Zaj, and Seyed Ahmadreza Afsari (C.A.)

Abstract: Rare-earth permanent magnet (PM) devices are increasingly facing challenges due to market monopolies. To mitigate these concerns, researchers have focused on reducing the use of rare-earth PMs while maintaining device performance. This study presents a novel hybrid structure for coaxial magnetic gears, combining the benefits of both magnetic and reluctance-based models. The proposed configuration delivers effective torque, reduced losses, and reliable performance at high speeds, all while minimizing magnet volume. The hybrid approach enhances high-speed performance, decreases the reliance on rare-earth magnets, and improves overall efficiency by incorporating reluctance principles into the inner rotor. In addition to new rotor section designs, three alternative hybrid rotor configurations are proposed. Particle Swarm Optimization algorithm is applied for optimization. ANSYS Maxwell and OptiSLang are used for electromagnetic simulation and optimization, and ANSYS Workbench is employed to assess mechanical performance. Unlike previously reported hybrid magnetic gears that rely solely on permanent-magnet-based torque production, the proposed topology combines permanent-magnet excitation and reluctance-based permeance modulation within a unified coaxial magnetic gear architecture.

Keywords: magnetic gear, hybrid rotor, reluctance rotor, PM rotor, finite element, torque density, cogging torque.

1 Introduction

AS technology advances, the demand for gears with higher performance and reliability continues to increase. Designing and manufacturing gears with high strength and reliability (especially for harsh environments characterized by high temperatures, extreme pressures, and severe corrosion) remains a significant challenge. The design process becomes even more complex due to the requirements for high load capacity, high speed, low friction, and extended service life. Addressing these engineering challenges in design, manufacturing, and related fields is therefore of critical importance. Despite these advancements, traditional mechanical gears—the earliest form of gear systems—rely on physical contact between teeth to transmit power. This direct contact leads to common issues such as wear, heat generation, and reduced service life. In applications demanding high precision, high rotational speed, and operation under specialized conditions, these problems become more pronounced. To overcome these limitations, magnetic gears (MGs) have emerged as a promising alternative. MGs transmit power using magnetic forces between moving components rather than physical contact. As a result, they offer advantages such as reduced wear, longer operational life, and improved performance across a wide range of applications in various industries including wind turbines [1], electric and hybrid vehicles [2], marine systems [3], and aerospace [4].

The surface-mounted permanent magnet coaxial magnetic gear (SPM-CMG), initially introduced in [5] (Fig. 1-a), represents the first model of MG. Its operation

Iranian Journal of Electrical & Electronic Engineering, YYYY.
Paper first received DD MONTH YYYY and accepted DD MONTH YYYY.
The authors are with the Faculty of Electrical and Computer Engineering, University of Kashan.
E-mail: madanchizaj@grad.kashanu.ac.ir
E-mails: afsari@kashanu.ac.ir
Corresponding Author: Seyed Ahmadreza Afsari.

is based on the magnetic field modulation principle. The three fundamental components of CMGs are the inner rotor, ferromagnetic pole pieces (modulators), and the outer rotor. In CMGs with radial magnetic orientations, permanent magnets (PMs) are mounted on the outer and inner surfaces of the inner and outer rotors, respectively. The ferromagnetic pole pieces modulate the magnetic fields generated by both rotors to control torque and speed. In [6], various types of magnets were investigated for CMG performance, including samarium-cobalt (SmCo), ferrite, neodymium-iron-boron (NdFeB), and Alnico. NdFeB magnets demonstrated the highest torque density (TD) when performance was the sole criterion, whereas Alnico magnets were preferred for their cost-effectiveness despite lower performance. This model's primary advantages include simplicity, high TD, and low cogging torque. However, surface-mounted PMs are susceptible to issues such as detachment at high speeds and increased eddy current losses within the magnets. To address these limitations, a CMG with interior permanent magnets (IPM-CMG) was developed [7] (Fig. 1-b). This design was especially suitable for high-speed applications, offering better magnet retention and allowing the use of more economical flat magnets. Nonetheless, the embedded PMs in the inner rotor can introduce unwanted harmonics, which increase output torque ripple. To counter this, [8] proposed V-shaped PM arrangements to enhance high-speed performance and reduce harmonic distortion. Further refinement of the IPM-CMG structure was made in [9], where the pole shape was optimized to minimize harmonic effects caused by the IPM layout. This optimization utilized a combination of the super formula function and pulse-width modulation techniques. Additionally, [10] introduced a flux-focusing PM arrangement for CMGs (Fig. 1-c), in which PMs are placed radially within the rotors. While this configuration can increase the effective PM volume or pole number, it may also lead to increased core losses [11].

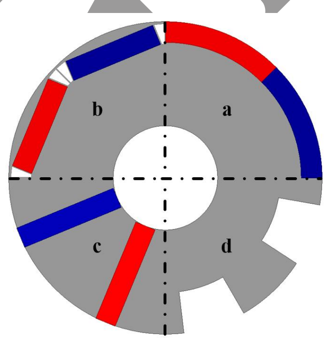

Fig 1. Inner rotor of (a) SPM-CMG, (b) IPM-CMG, (c) FF-CMG and (d) RMG.

Reluctance magnetic gears (RMGs) with salient rotors were introduced in [12], featuring a design where no magnets are placed in the high-speed rotor (Fig. 1-d). This topology is known for its simplicity, robustness, and the elimination of leakage flux in the inner rotor, leading to high efficiency at high speeds. A comparative study conducted in [13] analyzed the performance of RMGs versus SPM-CMGs. While findings confirmed that SPM-CMGs exhibit significantly higher TD, they also face challenges at high-speeds due to eddy current losses and mechanical limitations within the permanent magnets. In contrast, RMGs are well-suited for high speeds applications. To enhance their performance, an RMG with flux barriers (FBs) was proposed in [14], enabling improved operation through FB optimization. Additionally, [15] introduced a non-ferromagnetic core with iron teeth embedded on its surface to increase the torque density of RMGs. The use of rare-earth magnetic gears is increasingly threatened by factors such as excessive material consumption, price volatility, and supply chain instability driven by market monopolies. In response, researchers have explored alternative designs aimed at maintaining average torque while minimizing cogging torque by using fewer rare-earth magnets. One such approach, described in [16], introduced a hybrid V-shaped structure combining ferrite and rare-earth magnets for CMGs. In [17-18], other hybrid magnet concepts in coaxial magnetic gears have been explored by combining rare-earth and ferrite PMs in different arrangements to improve torque density while reducing cogging torque, iron losses, and overall material cost. By exploiting the complementary characteristics of high-energy rare-earth magnets and low-cost ferrite magnets, these designs achieve a balanced trade-off between electromagnetic performance and economic feasibility. In the context of electric machines, efforts to address this issue often involve integrating magnets into the rotor structures of synchronous reluctance motors to enhance both torque density and overall efficiency. Two notable methods have emerged: one embeds magnets within the flux barriers [19], while the other involves designing rotors with distinct magnetic and reluctance segments [20].

Although several hybrid magnetic gear topologies have been reported in recent years, including configurations employing different permanent magnet materials and alternative PM arrangements [16–18], the torque production mechanism in those designs remains entirely dependent on permanent-magnet excitation. In contrast, the proposed structure introduces a hybrid PM-reluctance magnetic gear in which two fundamentally different torque-production mechanisms are integrated within a single device. The PM section provides high torque density through magnetic excitation, whereas the reluctance section contributes torque through permeance modulation without requiring permanent magnets. This approach addresses an important gap in magnetic gear research by enabling a systematic reduction in rare-earth magnet consumption while preserving the main torque-producing harmonics. Furthermore, a common gear-ratio formulation is developed to enable the coexistence of PM and reluctance sections within the same coaxial magnetic gear. The proposed design therefore represents not only a new rotor geometry but also a new hybrid magnetic gear concept that combines the advantages of conventional PM and reluctance magnetic gears. This paper presents a novel CMG structure, in which the inner rotor incorporates both magnetic and reluctance sections. The primary objective is to reduce the use of rare-earth magnets in the inner rotor by utilizing reluctance-based torque generation, while maintaining or improving the overall torque density. Section I provides a brief literature review of CMGs. Section II explains the operating principles of CMGs and reluctance magnetic gears (RMGs) and introduces a unified gear ratio applicable to both configurations. In Section III, the proposed hybrid magnetic-reluctance CMG structure is introduced. To enhance the performance of the proposed design, new configurations are developed for each part of the rotor. Due to the fundamental differences in the operating principles of conventional CMGs and RMGs, directly incorporating PMs into a reluctance rotor is not feasible, which motivates the proposed hybrid magnetic–reluctance design.

2 Operation Principle

2.1 Conventional CMG

By entering the ferromagnetic pole-pieces, the magnetic fields generated by both the inner and outer PM rotors in CMGs form a dominant spatial harmonic based on opposing magnetic poles. In the appropriate harmonic order, these fields interact with corresponding harmonics of the other PM rotor. The primary magnetic flux flows radially through the outer rotor, ferromagnetic pole-pieces, air gaps, and the inner rotor core. This interaction facilitates torque transmission, causing the second rotor to rotate at a different speed and enabling gear functionality. The number of pole pairs in the space harmonic flux density produced by the high-speed or low-speed rotor can be determined using the following formula [5]:

$$\begin{aligned} &p_{m,k} = \left| mp + kn_s \right| \\ &m = 1,3,5,\ldots,\infty \\ &k = 0,\pm1,\pm2,\pm3,\ldots,\pm\infty \end{aligned} \tag{1}$$

where, n_s and p denote the number of stationary ferromagnetic pole-pieces and the number of pole pairs, m and k are constant pole number coefficients, respectively. Additionally, the rotational speed of the space harmonic flux density can be expressed as:

$$\Omega_{m,k} = \frac{mp}{mp + kn_s}\Omega_r \tag{2}$$

$$n_s = p_o + p_i \tag{3}$$

where, Ω_r , p_i, p_o are the rotational speeds, number of pole-pairs of inner and outer PM rotors, respectively. When, *m=1* and *k=-1* the dominant asynchronous spatial harmonic is achieved. To transfer torque at the harmonic speed, the number of pole pairs of the other rotor must satisfy Equation (3). Consequently, the gear ratio follows this relationship:

$$\begin{cases} G_r = -\dfrac{p_o}{p_i} & \textit{if modulator is stationary} \\ G_r = \dfrac{n_s}{p_i} & \textit{if outer rotor is stationary} \\ G_r = \dfrac{n_s}{p_o} & \textit{if inner rotor is stationary} \end{cases} \tag{4}$$

2.2 Reluctance MG

The operational principle of Reluctance MGs is largely similar to that of CMGs. In CMGs, ferromagnetic pole-pieces modulate the magnetic flux between the inner and outer PM rotors, producing alternating harmonics with varying pole counts and speeds. These harmonics interact with the other PM rotor to enable torque and speed conversion according to the gear ratio. In contrast, RMGs do not employ permanent magnets on the inner rotor. Instead, the primary focus shifts to the permeance distribution of the inner rotor's teeth, rather than its magnetomotive force (MMF). The radial magnetic flux flows through the inner rotor's teeth, air gaps, and ferromagnetic pole-pieces. This interaction results in torque transfer and causes the second rotor to rotate at a different speed. The pole-pair count and modulator count for the system can be calculated using the following formula [9]:

$$\begin{aligned} &\frac{k_a p_o' \omega_o + j_a n_s' \omega_s}{k_a p_o' + j_a n_s'} = \frac{k_b p_o' \omega_o + j_b p_r \omega_r}{k_b p_o' + j_b p_r} \\ &k_a = 1,\ k_b = 1,\ j_a = -1,\ j_b = 1 \end{aligned} \tag{5}$$

where, p_r, p_o and n_s represent the number of inner rotor teeth, the number of pole pairs in the outer rotor, and the number of ferromagnetic pole-pieces, respectively. The constants k_a, k_b, j_a and j_b are selected to maximize space harmonic amplitude. Furthermore, ω_o, ω_s and ω_r denote the rotational speeds of the outer rotor, ferromagnetic pole-pieces, and inner rotor, respectively. The system's gear ratio is then given by:

$$
\begin{cases} G_r = -\dfrac{2p'_o}{p_r} & \text{if modulator is stationary} \\ G_r = \dfrac{n'_s}{p_r} & \text{if outer rotor is stationary} \end{cases} \tag{6}
$$

$$
p'_o = \begin{cases} (G_{r,Int}\, p_r + 1)/2 & \text{for } G_{r,Int}\, p_r \text{ odd} \\ (G_{r,Int}\, p_r + 2)/2 & \text{for } G_{r,Int}\, p_r \text{ even} \end{cases}
$$

$$
n'_s = p_r + 2p'_o
$$

(7)

where, G_r and $G_{r,Int}$ are gear ratio and integer part of the gear ratio, when outer rotor is stationary.

2.3 Common Gear Ratio in Hybrid MG

Comparing the gear ratios of RMG and CMG, it is evident that with the same number of pole pairs on the outer PM rotor, the RMG achieves approximately twice the gear ratio of the CMG; consequently, directly integrating permanent magnets into the inner rotor of an RMG becomes impractical due to gear-ratio incompatibility. Therefore, combining the two mechanisms requires a segmented design: one segment operating under the CMG principle and another under the RMG principle to realize this concept, equations (4) and (6) show that setting the outer rotor as stationary in both CMG and RMG configurations with the same number of inner PM pole pairs and inner rotor teeth can yield an identical gear ratio. In this study, the proposed hybrid MG design adheres to the criteria established in [21] for wind turbine applications. Accordingly, the remaining pole-pair combinations satisfying these constraints are summarized in equation (8).

$$
\frac{n_s}{p_i} = \frac{n'_s}{p_r} \Leftrightarrow n'_s = n_s,\, p_i = p_r,\, p_o = 2p'_o \tag{8}
$$

$$
p_1 = p_i = 6
$$

$$
n'_s = n_s = 32
$$

$$
p_o = 26,\, p'_o = 13
$$

Rotor designs for dual reluctance-magnetic systems can be implemented using three configurations: First, the rotor consists of one reluctance segment and one magnetic segment placed side by side (Fig. 2-a). Second, the rotor features two magnetic segments with a reluctance segment positioned between them (Fig. 2-b). Third, the rotor includes two reluctance segments with a magnetic segment located between the two reluctance sections (Fig. 2-c). In the next section, new designs are proposed for both the reluctance and magnetic segments. In the absence of an isolator layer, the PM and reluctance sections are directly connected along the axial direction, leading to strong axial flux leakage and unintended magnetic coupling between the two sections. This interaction distorts the local flux distribution, increases saturation at the interface, and reduces the effective torque contribution of each section. To address this issue, a non-ferromagnetic isolator layer is introduced between the PM and reluctance rotor cores. The isolator interrupts the axial magnetic path and significantly suppresses flux leakage between the sections, thereby improving flux confinement and stabilizing torque production. Although the isolator separates only the rotor cores and not the air gaps, and some air-gap flux interaction remains, it effectively mitigates axial interference and enhances the electromagnetic robustness of the hybrid magnetic gear design. Fig. 3 exhibits the distributions of flux line resulting in the proposed configurations with and without isolation layer.

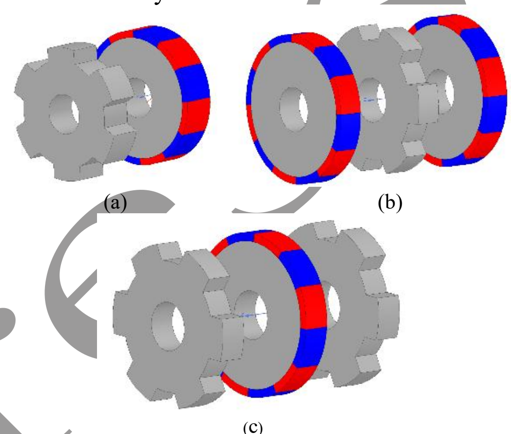

Fig 2. The proposed hybrid reluctance-PM MG structure (a): model 1, (b): model 2, (c): model 3

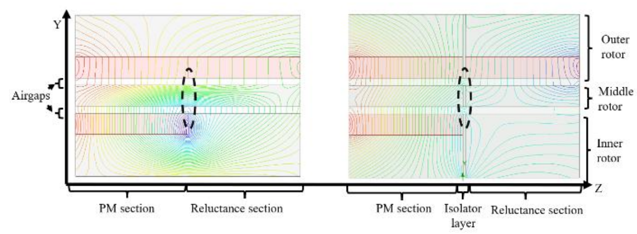

Fig 3. Flux lines distributions between PM and Reluctance sections of proposed model (left) without isolation layer and (right) with isolation layer

3 Design and optimization of hybrid reluctance-PM MG models

3.1 *Proposed magnetic rotor design*

As previously discussed, surface PM (SPM) structures are unsuitable for high-speed operations due to centrifugal forces and elevated magnet losses. Consequently, interior PM (IPM) or flux-focusing (FF) structures are more suitable for high-speed applications. In this study, a flux-focusing configuration is adopted for the proposed design. Fig. 4 illustrates the magnetic flux density distribution in a basic FF structure. A key issue with this model is the non-uniform magnetic flux distribution on the rotor surface. It has been observed that the regions adjacent to the magnets (identified as area I) exhibit significantly higher flux density compared to the middle sections between the magnets (identified as area II). This uneven distribution leads to an increase in subharmonic components of the magnetic field in the air gap, which in turn contributes to cogging torque in MG systems. Additionally, area III, as marked in the figure, reveals flux leakage paths that cause magnetic energy losses, resulting in decreased output torque. Furthermore, the formation of area IV (where magnetic flux is negligible) not only reduces the overall rotor weight but also enhances rotor cooling by allowing airflow through that region.

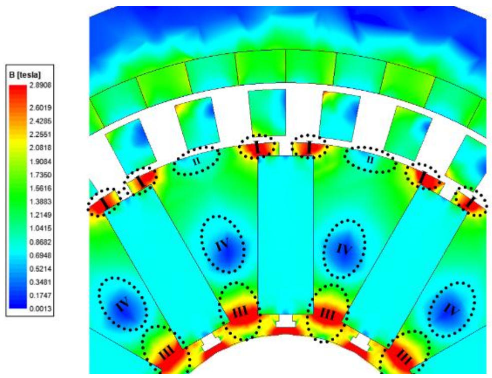

Fig 4. Magnetic flux density distribution of a conceptual basic FF-CMG

Reference [22], based on the magnetomotive force equation (9), modifies the airgap permeance to achieve a more sinusoidal flux density distribution in the air gap of a flux-focusing PM (FF-PM) synchronous machine. In this context, ϕ, R, and P denote the magnetic flux, reluctance, and airgap permeance, respectively, while μ_r, μ_0, A, and l represent the relative permeability of the material, the permeability of air, the cross-sectional area, and the flux path length.

$$MMF = R \times \phi$$
$$R = \frac{1}{P} = \frac{l}{\mu_0 \mu_r A} \tag{9}$$

A sinusoidal flux distribution can be realized by introducing recesses on the rotor surface, forming protrusions that adjust the airgap permeance. Inspired by this approach, the present study proposes a rotor structure based on decentralized circles to enhance the flux distribution across both the rotor surface and the air gap. In the proposed configuration, the airgap permeance near the magnets is reduced to guide the magnetic flux generated by the magnets toward the intermediate regions. This yields a more balanced and uniform flux profile. To address the issue of leakage flux within the rotor's inner regions, a dome-shaped flux barrier is introduced. This feature redirects leakage flux from the interior toward the rotor surface, as illustrated in Fig. 5. The final proposed structure comprises decentralized circles on the rotor surface and a dome-like flux barrier. The corresponding rotor geometry and design parameters are depicted in Fig. 6 and detailed in Table 1.

The electromagnetic function of the proposed decentralized circles is to reshape the local airgap permeance distribution. By increasing the local reluctance in regions where magnetic flux concentration is naturally high, the flux is redistributed to neighboring low-flux regions, resulting in a more uniform air-gap flux density profile. In addition, the dome-shaped flux barrier suppresses internal leakage flux paths and redirects magnetic flux toward the air gap. These two effects jointly strengthen the dominant torque-producing harmonic while reducing high-order harmonics associated with cogging torque and torque ripple.

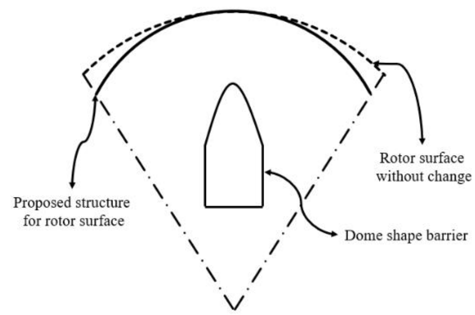

Fig 5. The decentralized and Dome shape barrier

Table 1. Design parameters PM rotor

Parameters	Symbols	Range
PM's length (mm)	L_{pm}	*19-21*
PM's widths (mm)	W_{pm}	*6-9*
Radius of decentralized circle (mm)	R_1	*28-33*
PM distance from centre (mm)	R_2	*29-31*
Dome-shape barrier distance from centre (mm)	R_3	*20-25*
Dome-shape barrier's height (mm)	H_1	*15-20*
Dome-shape barrier's width (mm)	W_b	*3-6*
End barrier's length (mm)	L_1	*3-5*

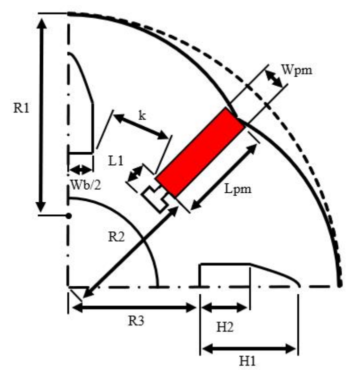

Fig 6. Design parameters of PM rotor

3.2 Proposed reluctance rotor design

In this study, a novel reluctance rotor structure is introduced, drawing upon the concept presented in reference [23], which suggested an alternative geometry for the rotor of a switched reluctance motor. The new structure incorporates crescent-shaped flux barriers for application in reluctance-based magnetic gears. Instead of large gaps between adjacent teeth, the proposed configuration allows a gradual change in reluctance encountered by the magnetic flux, contributing to a more sinusoidal flux distribution in the air gap. The grooves in the proposed model exhibit an elliptical profile, which can be optimized to increase groove reluctance. Each flux barrier is composed of two elliptical arcs that serve to direct the incoming magnetic flux efficiently. The optimal number of such flux barriers must be determined to achieve maximum torque output. A comparative analysis between a conventional toothed-slot structure and the proposed design is shown in Fig. 7, while Fig. 8 presents the detailed geometrical parameters of the proposed model.

Unlike conventional slot-tooth reluctance rotors, the proposed crescent-shaped barriers introduce a gradual permeance transition along the rotor circumference. This smoother permeance variation reduces abrupt magnetic field changes and weakens undesirable harmonic components in the air gap. Consequently, the magnetic field distribution becomes smoother, and the resulting torque waveform exhibits lower ripple while preserving the torque-producing harmonics.

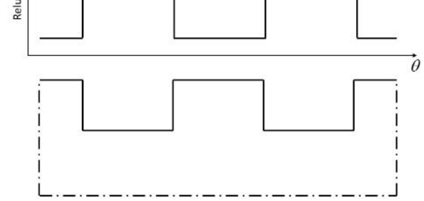

(a)

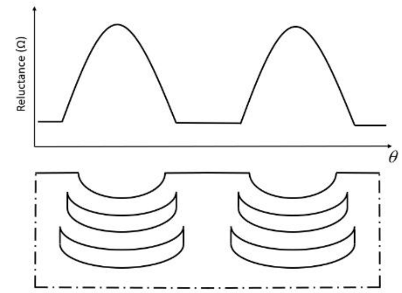

(b)

Fig 7. Reluctance comparison of (a) simple teeth and slot model and (b) proposed model

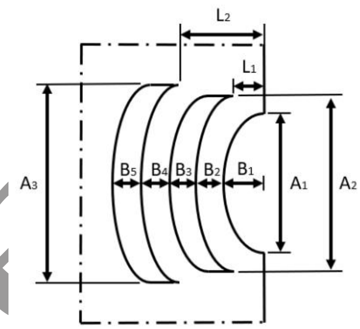

Fig 8. Design parameters of reluctance rotor

Preliminary simulations suggest that incorporating a single crescent-shaped flux barrier layer is sufficient for effective performance, as adding a second layer does not yield significant improvements. The final design parameters of the reluctance rotor are summarized in Table 2.

Table 2. Design parameters of reluctance rotor

Parameters	Symbols	Range
Slot opening (mm)	*A1*	*12-16*
Slot depth (mm)	*B1*	*6-4*
First moon shape barrier's width (mm)	*A2*	*10-18*
First moon shape barrier's thickness (mm)	*B3*	*1-3*
First moon shape barrier's distance from surface (mm)	*L1*	*2-4*
First moon shape barrier's distance from slot (mm)	*B2*	*1-3*
Second moon shape barrier's width (mm)	*A3*	*10-18*
Second moon shape barrier's thickness (mm)	*B5*	*1-3*
Second moon shape barrier's	*L2*	*6-10*

distance from surface (mm)		
Second moon shape barrier’s distance from first moon barrier (mm)	*B4*	*1-3*

The purpose of introducing the reluctance segment is not merely to replace a portion of the permanent magnets, but to establish an additional torque-production path based on permeance modulation. Consequently, part of the transmitted torque is generated without direct reliance on permanent-magnet excitation, leading to improved torque-to-magnet-volume characteristics and enhanced suitability for high-speed operation.

3.3 Optimization

Genetic Algorithms (GA), which employ techniques such as variable selection, crossover, and mutation, have long been utilized to optimize the design of electrical machines. Unlike some optimization methods that tend to converge to local optima, GA excels at exploring the global search space, offering a distinct advantage in solving nonlinear optimization problems. However, despite their widespread application, GAs may not always provide globally optimal solutions (particularly in high-dimensional or complex design spaces) and can be computationally intensive. Particle Swarm Optimization (PSO) has emerged as a reliable alternative, offering a population-based optimization framework that is computationally efficient and relatively simple to implement. PSO has demonstrated strong performance in addressing high-dimensional and nonlinear problems, often outperforming GA in terms of solution speed and consistency. Studies have demonstrated the effectiveness and robustness of PSO in multi-objective optimization tasks, such as reducing component size while improving performance [16]. In this study, PSO is employed to achieve optimal performance in the design of the proposed MG. The PSO flowchart is illustrated in Fig. 9.

PSO was selected as the optimization tool due to its strong convergence characteristics, low implementation complexity, and successful application in numerous electromagnetic design optimization problems reported in the literature. Since the focus of this study is the development of a hybrid magnetic gear topology rather than the evaluation of optimization algorithms, alternative metaheuristic methods were not investigated.

Simulations were conducted using Ansys optiSLang 2021 on a system running Windows 10 with an Intel Core i7 4980HQ processor, 8 GB of RAM, and a 120 GB SSD. The selected PSO parameters shown in Table 3 fall within commonly accepted ranges reported in electric machine optimization literatures and were chosen to ensure stable convergence and repeatability of the optimization results.

Table 3. Table III: Key PSO parameters

Parameter	Symbol	Value	Description
Swarm size	N_p	30	Number of particles in the swarm
Inertia weight	ω	0.9 → 0.4	Linearly decreasing to balance exploration and exploitation
Cognitive coefficient	c_1	2.0	Attraction toward personal best position
Social coefficient	c_2	2.0	Attraction toward global best position
Maximum iterations	N_{iter}	200	Termination criterion
Velocity limit	(V_{max})	20% of variable range	Prevents excessive particle movement

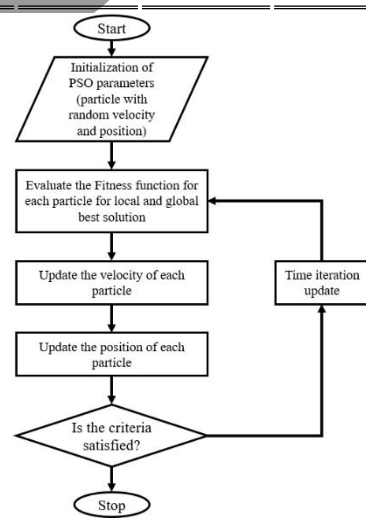

Fig 9. PSO flowchart

3.4 Proposed magnetic rotor optimization

In the magnetic rotor model, three primary optimization objectives are considered (equation (9)): (1) increasing average torque and torque density (T_{avg}), (2) reducing cogging torque ($T_{p\text{-}p}$), and (3) minimizing the volume of magnets used (V_{pm}). Due to the conflicting nature of these objectives (namely torque, ripple percentage, and magnet volume) a trade-off must be made between maximizing torque and minimizing magnet usage. The presented objectives are per-united for better understanding; the reference values are based on the result of the optimal initial design. Consequently, Pareto-optimal solutions are more appropriate in this context, as finding a single definitive optimum is improbable. This leads to a set of distinct optimal design alternatives.

$$O.F. = \frac{T_{avg}^{actual}}{T_{avg}^{ref}} \quad \frac{1}{\dfrac{\%T_{cog}^{actual}}{\%T_{cog}^{ref}}} \quad \frac{1}{\dfrac{V_{pm}^{actual}}{V_{pm}^{ref}}}$$

(9)

The Pareto front shown in Fig. 10 consists of 282 non-dominated design candidates obtained using per-unit normalized objectives. Among these solutions, the most favorable candidates correspond to average torque values of approximately 17–20 Nm, cogging torque below 5%, and maintaining the magnet volume relative to the baseline design. In per-unit terms, these designs are clustered in the region of high T_{avg} (≈1.0–1.3 pu), low T_{cog} (below 0.3 pu), and low V_{pm} (≈1.0 pu). This concentration demonstrates the effectiveness of the Pareto-based optimization in identifying balanced trade-offs between torque performance, cogging torque suppression, and magnet volume reduction. To achieve an ideal balance between performance metrics, the configuration yielding the highest Objective Function (OF) score was designated as the optimal solution. Both the original and the proposed design solutions are depicted in Fig. 11.

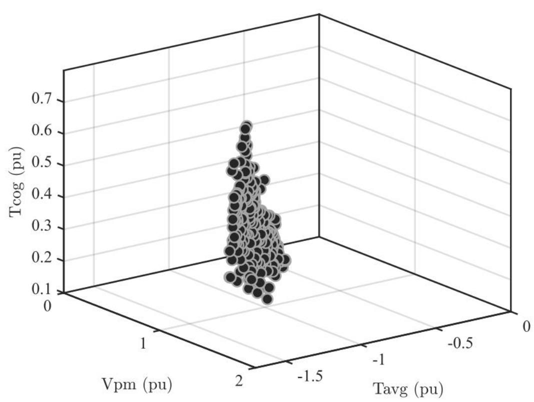

Fig 10. Three-dimensional Pareto front of the PM rotor optimization showing the trade-off between T_{avg} *(pu)*, T_{cog}*(pu)*, and V_{pm}*(pu)*.

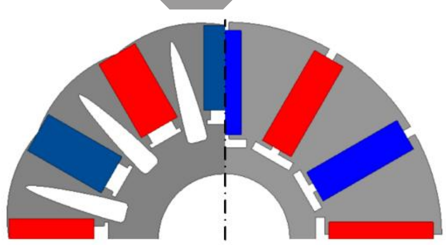

Fig 11. The optimal (right) initial and (left) proposed PM rotor design

As illustrated in Fig. 12, high-speed and low-speed rotor torques are obtained with average values of 17.5 Nm and 94.5 Nm in the 2D model, and 15 Nm and 79.3 Nm in the 3D model, respectively. The approximate 18% discrepancy between the 2D and 3D results is attributed to end effects in the 3D simulation. Both rotor types demonstrate low cogging torque percentages (2.7% and 2.4%, respectively) while using the same magnet volume. Table 4 presents a comparison of the outcomes for both the initial optimized model and the proposed design. The modified design achieves a 71.1% reduction in cogging torque and a 28.6% increase in torque compared to the original.

Fig. 13 presents tangential and radial magnetic flux densities within the air gap. Compared to the initial model, the proposed design demonstrates significant enhancements in flux distribution for both radial and tangential components. Notably, the radial flux distribution becomes smoother, exhibits fewer fluctuations, and presents more uniform characteristics, effectively minimizing ripple and irregularities. These improvements contribute to better system reliability and efficiency by directly lowering ripple and ensuring consistent torque output. Additionally, while the tangential flux distribution shows minor amplitude fluctuations at specific angular positions, the proposed model maintains a uniform flux pattern. This uniformity becomes increasingly important since tangential components are the primary source of torque generation. The enhanced smoothness and stability of the tangential flux in the proposed design reduce undesirable ripple and further improve torque quality. The FFT analysis of the air-gap flux density reveals a significant improvement in the spectral quality after optimization. The dominant torque-producing harmonic (order 6) shows a clear enhancement in the radial flux component (Br), increasing from approximately 0.35 T to 0.38 T. Crucially, the optimization has successfully suppressed high-order parasitic harmonics (orders 17 to 19), which are primary contributors to torque ripple and eddy current losses. While the tangential component (B_θ) remains relatively stable, the overall reduction in harmonic distortion and the strengthening of the fundamental component demonstrate that the proposed PM geometry effectively focuses magnetic energy into the working harmonic, leading to higher torque density and smoother operation. Fig. 14 displays the graphical representation of flux density and flux lines, demonstrating that the proposed model maintains performance and stability by adjusting flux distributions and minimizing flux amplitude variations. The static torque THD decreased from 54.7% in the base optimized model to 50.9% in the proposed optimized model, indicating an improvement of 3.8%.

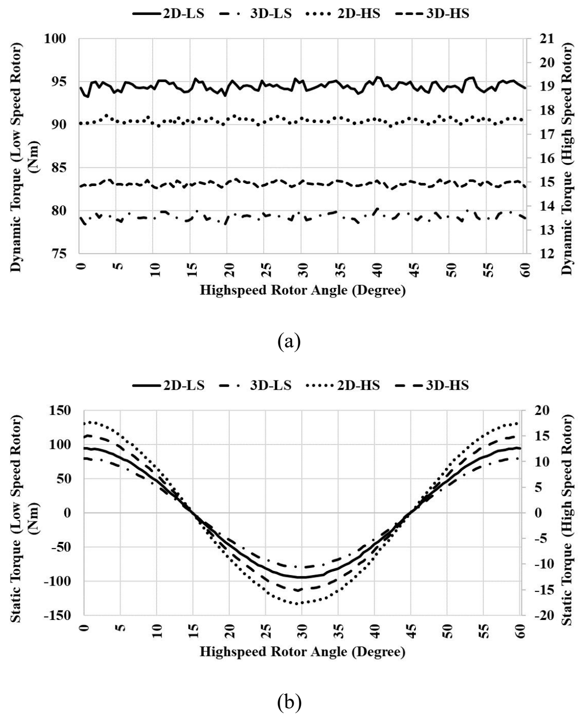

Fig 12. (a): Dynamic torque result and (b): Static torque result of PM rotor design regarding the highspeed rotor angle.

Table 4. Comparison between the optimal initial design and the optimal proposed PM rotor design

Results	Opt. initial design	Opt. proposed design	Changes
High-speed rotor torque (Nm)	13.6	17.5	28.6%
Low-speed rotor torque (Nm)	72.5	94	29.6%
High-speed Cogging torque (%)	9.5	2.7	-71.5%
Low-speed Cogging torque (%)	3.8	2.4	-36.8%
PM volume of inner rotor (mm^3)	109500	109500	-
THD of highspeed rotor static toque (%)	54.7	50.9	-3.8
O.F.	1	4.5	-

The FFT spectrum confirms that the optimization process selectively strengthens the fundamental torque-producing harmonic while suppressing several high-order components associated with torque ripple. In particular, the 6th-order harmonic, which is primarily responsible for torque transmission in the PM magnetic gear, exhibits a noticeable increase in amplitude after optimization. Simultaneously, the amplitudes of the 17th–19th harmonics are reduced. Since these high-order harmonics do not contribute significantly to average torque production and mainly generate pulsating torque components, their suppression directly contributes to the observed reduction in cogging torque and torque ripple.

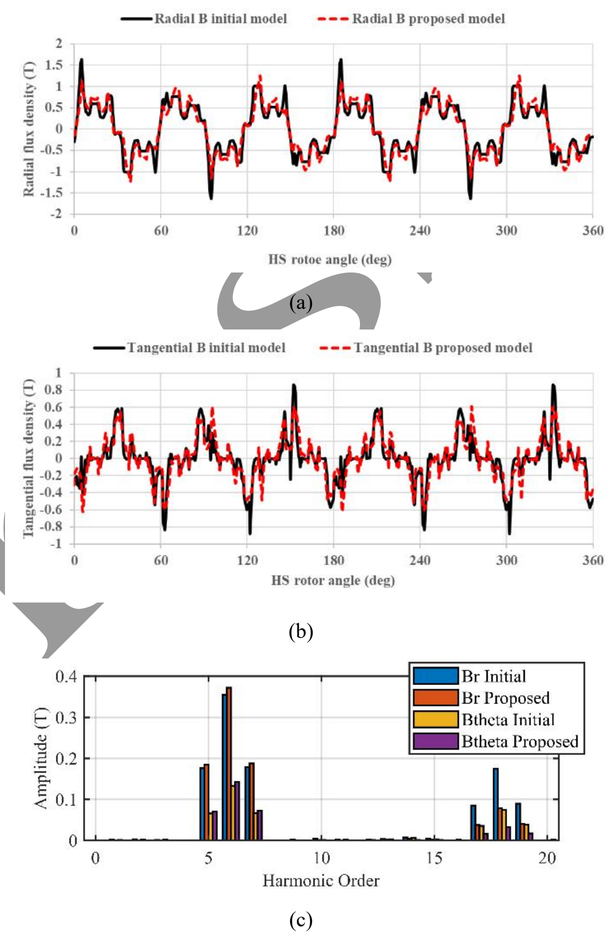

Fig 13. Magnetic flux density in the inner air gap proposed PM design (a): radial component, (b): tangential component and (c): FFT analysis results

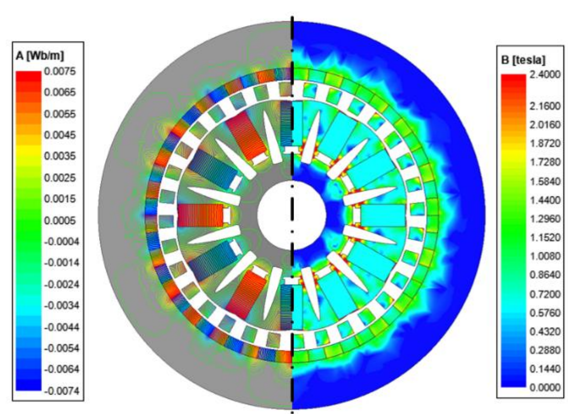

Fig 14. The distribution of flux density (right) and magnetic potential lines (left) in PM rotor structure.

3.5 Proposed reluctance rotor optimization

Since the reluctance model does not include magnets, the optimization goal is to increase the average torque while reducing cogging torque. Due to the differences in ripple percentage and average torque, the Pareto method has been employed for this optimization, as it allows for a more comprehensive and wide-ranging view of trade-offs. The objective functions are expressed in per-unit form to improve clarity, with the reference values derived from the optimal initial design. The O.F. is as follows:

$$O.F. = \frac{T_{avg}^{actual}}{T_{avg}^{ref}} \cdot \frac{1}{\dfrac{\%T_{cog}^{actual}}{\%T_{cog}^{ref}}} \tag{10}$$

Fig. 15 shows the Pareto front obtained from the multi-objective optimization, plotted with the normalized average torque, T_{avg} *(pu)*, on the horizontal axis and the normalized cogging torque, T_{cog} *(pu)*, on the vertical axis. The Pareto-optimal solutions form a curved front extending approximately from $T_{avg} = -1.02$ to -0.94 *pu* and T_{cog} = 0.65 to 0.95 *pu*. The leading edge of the distribution, indicated by the black boundary line, represents the non-dominated designs that provide the best trade-off between maximizing average torque magnitude and minimizing cogging torque. In total, 1,349 Pareto-optimal designs were identified. Among these, designs corresponding to an output torque range of 1.81–1.83 Nm and a tooth torque contribution between 13.5% and 14.5% are considered the most favorable, as they are located close to the Pareto front while maintaining a balanced compromise between torque performance and cogging torque reduction. The final optimal configuration was selected based on the maximum value of the defined O.F., ensuring the best trade-off between the target performance indicators among all pareto front designs. The optimal initial and proposed designs are depicted in Fig. 16.

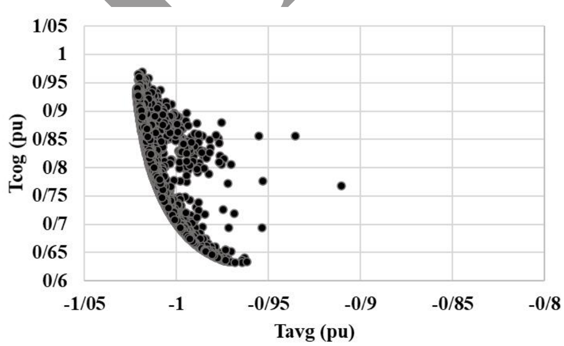

Fig 15. The resulted pareto front of reluctance design

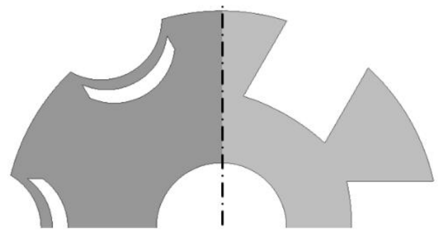

Fig 16. The optimal (right) initial and (left) proposed reluctance design

As shown in Fig. 17, in the 2D model, the average torque values for the high-speed and low-speed rotors are 1.82 Nm and 9.8 Nm, respectively. In contrast, in the 3D model, these values are 1.62 Nm and 8.9 Nm. This approximate 9% reduction is attributed to the consideration of end effects in the 3D model. However, the impact of end effects is less significant in the reluctance model than in the magnetic model, due to the absence of magnets. The high-speed and low-speed rotors have cogging torque percentages of 13.9% and 5.5%, respectively. Table 5 compares the results of the initial optimized model and the newly proposed design with the same PMs. The efficiency of the proposed design is evidenced by a 72% reduction in cogging torque, while maintaining a comparable average torque, after implementing the suggested modifications. The static torque THD decreased from 54.2 %in the base optimized model to 51.4 %in the proposed optimized model, indicating an improvement of 3.6%.

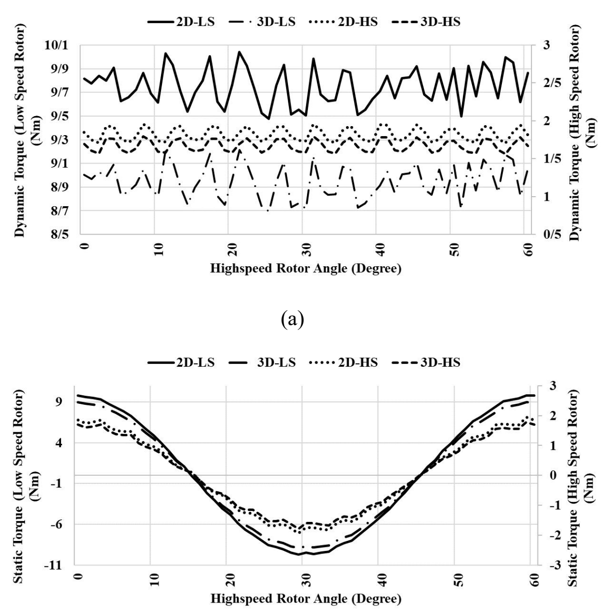

(b)

Fig 17. (a) Dynamic torque and (b) Static torque results of reluctance rotor MG design regarding the highspeed rotor angle.

Table 5. Comparison between the optimal initial design and the optimal proposed reluctance rotor design

Results	Opt. initial design	Opt. proposed design	Changes
High-speed rotor torque (Nm)	1.81	1.82	0.5%
Low-speed rotor torque (Nm)	9.6	9.8	2%
High-speed Cogging torque (%)	19.3	13.9	-72%
Low-speed Cogging torque (%)	9.3	5.5	59%-
THD of highspeed rotor static toque (%)	55.2	51.4	-3.8%
O.F.	1	1.4	

Both designs use a reluctance rotor, as illustrated in Fig. 18, where increasing magnetic flux density plays a key role in improving torque generation and overall efficiency. The proposed model (indicated by the dashed red line) achieves greater magnetic flux density across most of the angular range in the radial flux distribution and clearly outperforms the original model (black solid line). This increase in flux density enhances the rotor's torque capability, particularly since radial flux is crucial for generating the magnetic forces required for torque production. Furthermore, the proposed model demonstrates smoother flux distribution, reducing oscillations that could impair performance consistency. Additionally, the proposed model yields higher flux density in terms of tangential flux distribution, which directly contributes to improved torque output. Effective flux utilization and smoother operation are further supported by reduced tangential flux pattern variations. The proposed design significantly enhances performance by promoting stronger and more consistent flux distributions in both radial and tangential directions. These improvements establish the suggested model as a viable solution for high-performance applications, offering both greater torque and more stable, efficient operation. The FFT spectrum of the air-gap flux density for the reluctance segments demonstrates the efficacy of the proposed flux-barrier optimization. The dominant torque-producing harmonic at the 13th order (and its secondary peak at the 19th order) shows a noticeable increase in amplitude for the B_r in the proposed design compared to the initial geometry. This enhancement indicates a higher saliency ratio and improved permeance modulation. Furthermore, the optimization has effectively maintained or slightly reduced the parasitic sub-harmonics across the spectrum. By focusing the magnetic flux into the working harmonic orders, the proposed reluctance rotor contributes more effectively to the overall torque production while minimizing the potential for localized saturation, thereby justifying the hybrid architecture's superior performance. Fig. 19 presents detailed comparisons of the flux density and flux lines.

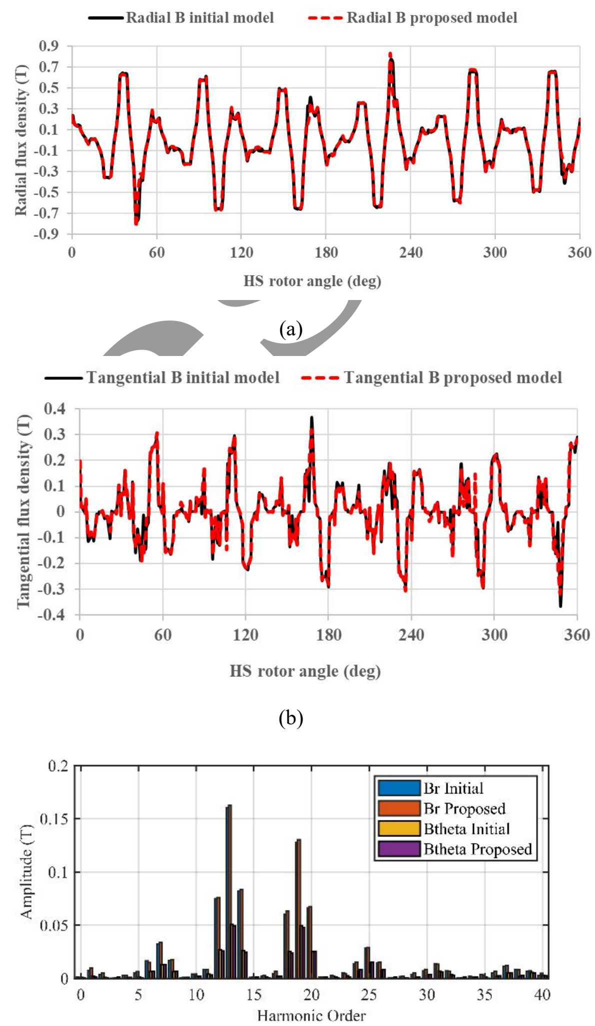

Fig 18. Magnetic flux density in the inner air gap proposed reluctance design (a) radial component, (b) tangential component and (c): FFT analysis results

For the reluctance rotor, the FFT analysis reveals that the optimization process improves the effectiveness of permeance modulation. The amplitudes of the dominant working harmonics (13th and 19th orders) increase after optimization, indicating stronger saliency-induced flux modulation. At the same time, lower-amplitude parasitic harmonics remain unchanged or are slightly reduced. This redistribution of harmonic content toward the torque-producing orders explains the simultaneous improvement in average torque and reduction in harmonic distortion.

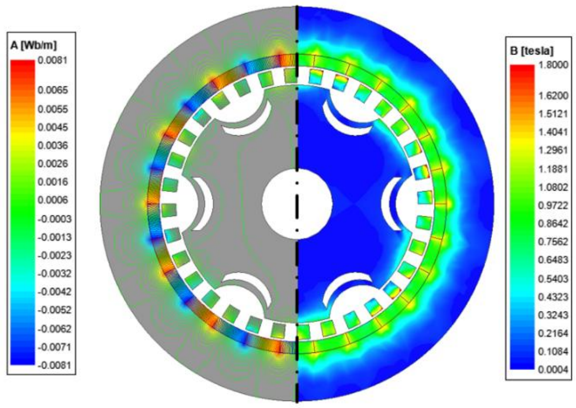

Fig 19. The distribution of flux density (right) and magnetic potential lines (left) in reluctance rotor design

3.6 Loss comparison analysis

In magnetic gears, due to the absence of physical contact, all losses are similar to those found in electric machines. However, in the two proposed types of magnetic gears, the absence of winding and an electrical power source eliminate AC and copper losses. The primary sources of loss in magnetic gears are core losses (such as hysteresis and eddy current losses) and magnet losses. Rotor core losses and PM eddy current losses in coaxial magnetic gears have been previously investigated using finite element analysis and validated through analytical loss modeling, including the consideration of sub-harmonic effects and flux barrier structures for loss reduction [24]. In this paper, finite element method (FEM) is used to evaluate the combined loss and efficiency and can be obtained as [24]:

$$W_{magnet} = \sum_n \left(\int \frac{|J_n|^2}{2\sigma} dv \right)$$
$$W_{core} = \sum_n \left(\int \left(A_e (nf)^2 B_m^2 + A_h (nf) B_m^2 \right) dv \right) \quad (11)$$

where J_n and σ are the amplitude of nth time-harmonic ECs and the conductivity, f is the frequency of the flux, B_m is the time-harmonic flux density at each finite element, A_h and A_e are the hysteresis and eddy current loss coefficients, respectively.

Fig. 20 presents the loss analysis and efficiency performance across a speed range of 0–10,000 rpm. At low speeds (below 2,000 rpm), the total losses in both the PM and reluctance models remain minimal. However, losses in the PM MG structure increase significantly at high speeds, reaching approximately 500 W at 10,000 rpm, whereas the reluctance design maintains much lower losses (around 50 W) at the same speed. This indicates that the PM model is more sensitive to speed due to eddy current and hysteresis losses in its magnets, while the reluctance model benefits from its magnet-free rotor, resulting in lower overall losses. At lower speeds (up to 2,000 rpm), the PM design demonstrates higher efficiency, exceeding 99.5%, compared to the reluctance model's efficiency of around 98.5%. However, as speed increases, the PM model's efficiency decreases steadily, dropping to 97.2% at 10,000 rpm, while the reluctance model remains more stable (around 96.5% at 6,500 rpm and improving to 97% at 10,000 rpm). Hence, although the PM model delivers higher efficiency at lower speeds, it suffers from increased losses and efficiency degradation at high speeds. In contrast, the reluctance model offers consistent performance with significantly lower losses, making it more suitable for high-speed applications. It should be noted that in these results only the electromagnetic losses have been observed and mechanical loss is not included.

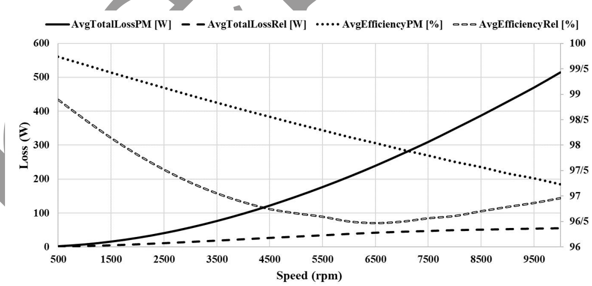

Fig 20. Loss and efficiency of proposed designs in different speeds

4 Hybrid PM-reluctance MG design

4.1 Electromagnetic analysis

Following the optimization of the proposed designs for the magnetic and reluctance sections, the performance of the enhanced hybrid PM-reluctance rotor is analyzed. All electromagnetic analyses in this study were carried out using a 3-D FEM developed in ANSYS Electronics Desktop 2021 R1. A 3D magnetostatic solver was employed to accurately capture the spatial magnetic field distribution, torque production, and flux interaction between the magnetic and reluctance sections of the proposed gear. The model consisted of 826,473 finite elements, with adaptive mesh refinement applied to critical regions, including the air gaps, magnet interfaces, flux barriers, and modulating pole pieces, where high field gradients are present. Magnetic insulation boundary conditions were imposed at the outer boundary of the computational domain to prevent flux leakage, while mechanical motion was modeled through relative angular displacement between the rotors. Mesh convergence was verified by monitoring torque variation, and the final mesh density was selected such that further refinement resulted in less than 1% change in the computed torque. This modeling approach ensures sufficient numerical accuracy and reliability for performance evaluation of the proposed magnetic gear configurations. As mentioned earlier, three configurations of this rotor have been introduced, now updated based on optimized designs, as shown in Fig. 21. To achieve optimal performance, the starting point of each segment must be adjusted according to the maximum allowable space, as determined by static testing. In this study, the length of the magnetic section (denoted as Z_{length_PM}) is considered an independent variable, while the total gear length (L) remains constant. The difference between the overall length and the magnetic section determines the reluctance section length. To prevent magnetic flux leakage, a 1mm thick non-ferromagnetic insulating plate is placed between the magnetic and reluctance sections.

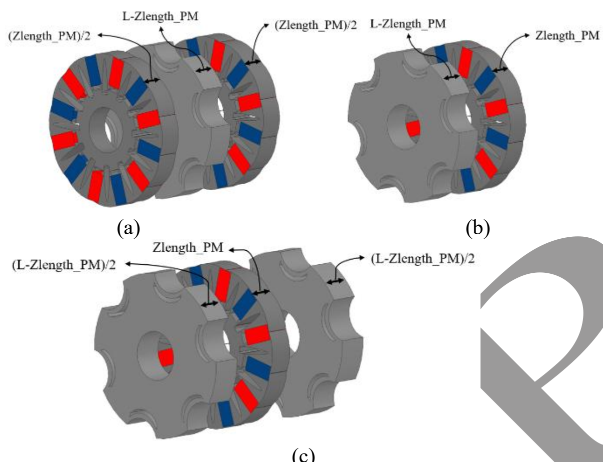

Fig 21. Exploded view of proposed configuration (a) model 1 (b) model 2 (c) model 3

In this study, the total gear length is fixed at 50 mm, and the magnetic section's length is varied in 5 mm increments from 10 mm to 40 mm. Thus, the reluctance section length is calculated by subtracting the magnetic section and insulating plate thickness from the total gear length. Fig. 22 shows the torque for each configuration, plotted against magnetic section length. The torque of the three proposed models is compared with that of standalone magnetic and reluctance rotors. As the magnetic section length increases, the performance of the proposed models improves. Lower torque at shorter magnetic section lengths is due to the dominance of the reluctance section, which yields lower average torque. Additionally, magnetic flux leakage under these conditions causes the torque to drop below that of a full magnetic rotor, as seen in the first model. The second and third models exhibit higher torque than the full magnetic rotor when the magnetic section length reaches 20 mm. However, the torque in these models remains below that of the combined torque of standalone magnetic and reluctance rotors. The third model, in which the reluctance section is placed on the gear's outer side (where end effects are less pronounced), generates higher torque than the combined standalone models beyond 20 mm, achieving on average 6% to 12% more torque than the other proposed configurations.

The combined torque of the hybrid PM–reluctance magnetic gear is lower than the sum of the standalone models due to nonlinear flux interaction in the shared magnetic circuit. From a harmonic viewpoint, the PM and reluctance sections do not operate as completely independent torque-producing units because they share a common air-gap magnetic field. The PM section mainly contributes the dominant working harmonics, while the reluctance section modifies the permeance distribution and introduces additional modulation harmonics. Consequently, a portion of the magnetic energy is redistributed among the available harmonic components rather than being linearly superimposed. The proposed isolator layer and optimized geometry reduce undesirable harmonic interaction and help concentrate magnetic energy in the principal torque-producing harmonics, thereby improving the overall electromagnetic utilization of the hybrid structure. Although a non-ferromagnetic insulating layer separates the rotor cores, it does not isolate the air gaps, allowing limited flux interaction through the common air-gap region. This leads to flux redistribution, preventing linear torque superposition. The effect is most pronounced when the magnetic section is short and the system is dominated by the reluctance part, since the PM section—having a stronger influence on torque production—cannot fully establish its optimal flux pattern. As the magnetic section length increases, flux interaction is reduced and the hybrid torque approaches that of the standalone magnetic gear, as shown in Fig. 22.

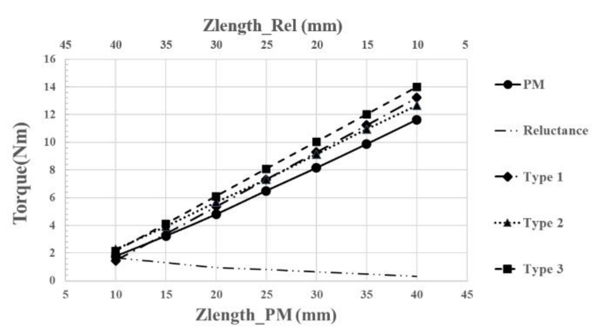

Fig 22. Torque of different MG configuration in different PM MG length

Fig. 23 illustrates the torque-to-magnet volume ratio of the inner rotor. At a magnetic section length of 10 mm, the second model achieves the highest torque-to-magnet volume ratio. Beyond 15 mm, all three proposed models outperform the fully magnetic rotor due to the addition of the reluctance section. Among these, the third model exhibits the highest torque-to-magnet volume ratio.

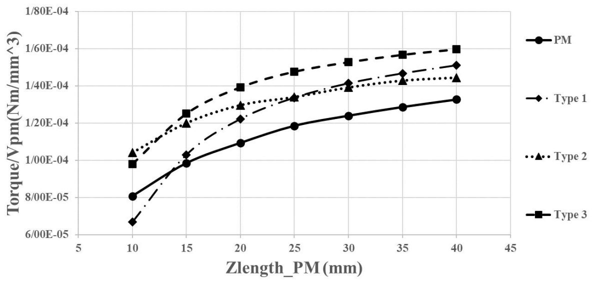

Fig 23. Torque-to-magnet volume ratio of different MG configuration in different PM MG length.

Fig. 24 shows the torque-to-total magnet volume ratio for the entire gear system (including both the inner and outer rotors). The fully reluctance rotor model, due to the absence of magnets in the inner rotor, exhibits a completely uniform trend, whereas the other models show an upward trend as the share of the magnetic section increases. At the beginning of the range, the fully magnetic model has a significantly higher torque-to-total magnet volume ratio compared to the proposed models. However, this difference gradually decreases, and beyond a magnetic section length of 35 mm, the third proposed model surpasses the fully magnetic model, demonstrating a higher torque-to-total magnet volume ratio.

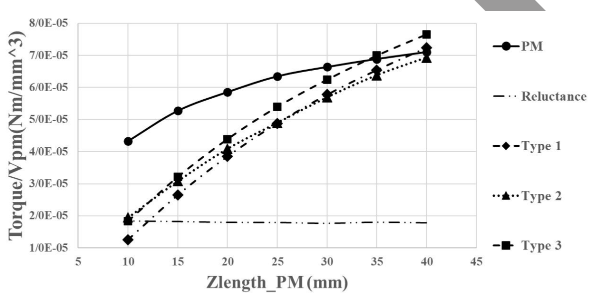

Fig 24. Torque-to-total magnet volume (inner and outer rotors) ratio of different MG configuration in different PM MG length

Table 6 compares the results of the hybrid PM-reluctance model with the optimal reluctance rotor model and the optimal PM rotor. The proposed hybrid model has 15% more torque per inner magnet volume than the magnetic integrated model. However, this model saves 20% and 10% respectively in magnet consumption in the inner rotor and magnet consumption in the entire gear and has only 7% less torque. Compared to an optimal experimental hybrid w-shaped IPM rotor magnetic gear (HWIPM) design [16], the proposed model achieves higher torque with comparable torque-to-magnet-volume ratios, demonstrating that it effectively balances torque performance and magnet efficiency. It should be noted that the axial length of the reluctance section in the proposed hybrid configuration is constrained by the fixed total gear length. When the reluctance section occupies a relatively short axial length, axial end effects become more pronounced, which limits its effective torque contribution. This behavior is consistent with the torque trends observed in Fig. 22, particularly when the magnetic section length is small and the system is dominated by the reluctance part. However, the reluctance section in the hybrid design is not intended to function as a standalone torque-producing element; instead, it serves to supplement torque while reducing permanent magnet volume. As the magnetic section length increases, the influence of end effects is reduced, and the overall torque performance of the hybrid configuration improves accordingly.

The three-dimensional magnetic flux density distribution of the optimized hybrid magnetic gear is illustrated on Fig. 25. As shown in the full and sliced views, the flux distribution remains within the linear operating region of the core material in most sections, with controlled saturation observed primarily at the pole tips and flux barrier edges. This visualization confirms the effective guidance of magnetic flux through the proposed rotor geometry and the minimal axial leakage between the PM and reluctance segments. The absence of significant flux concentration at the interface between the PM and reluctance sections indicates that local magnetic saturation is effectively controlled. This observation confirms that the non-ferromagnetic isolator successfully mitigates excessive axial coupling while maintaining the desired torque-producing flux paths. A summary of the main elements of the dual-rotor PM-reluctance MG is also provided on Fig. 26, emphasizing how the reluctance and magnetic sections are integrated to maximize performance.

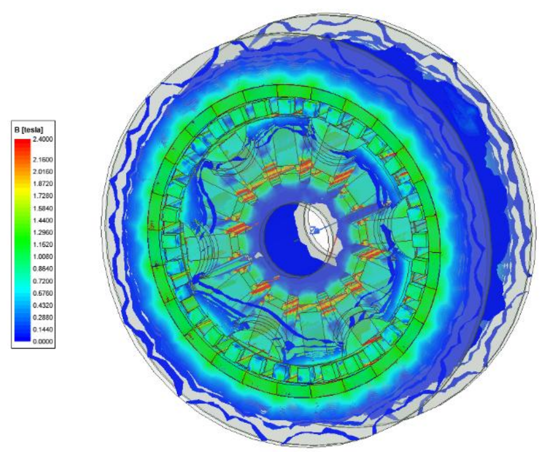

(a)

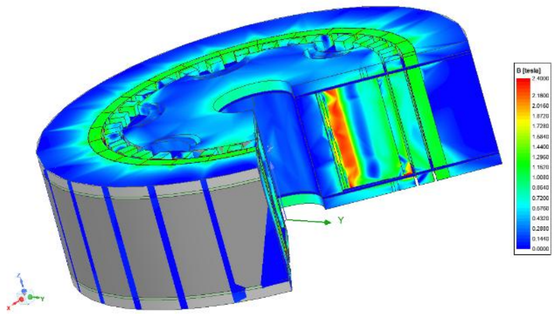

(b)

Fig 25. 3D flux density distribution of proposed model (a) full model and (b) ¾ sliced model

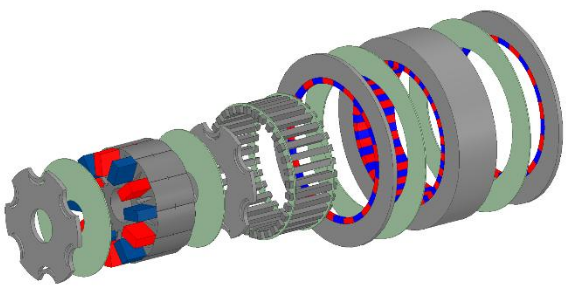

Fig 26. Exploded view of proposed model

4.2 Mechanical analysis

The mechanical performance of the proposed model is analyzed using ANSYS Workbench 2021 R1 to ensure structural integrity under operational conditions. For the rotor core material, M400-50A steel was selected (a widely used material in electric motor applications due to its favorable magnetic and mechanical properties). This steel offers a maximum tensile strength of 350 MPa, making it well-suited for high-stress applications. As illustrated in the stress analysis results (Fig. 27 and Table 6), the incorporation of the optimized reluctance segments not only enhances the magnetic flux distribution but also provides superior structural integrity. The proposed rotor can safely withstand rotational speeds of up to 28,943 rpm, providing a substantial safety margin for high-speed industrial applications. In contrast, the state-of-the-art HWIPM structure is limited to a maximum operating speed of 12,500 rpm.

Among the available magnetic gear topologies reported in recent literature, the HWIPM configuration represents the closest design philosophy to the proposed hybrid PM-reluctance structure because both approaches aim to improve magnet utilization while maintaining torque capability. Therefore, it was selected as the primary benchmark for performance evaluation.

Table 6. Comparison between the optimal PM MG, reluctance MG designs and the optimal proposed hybrid PM-reluctance MG design

Results	Fully magnetic model	Fully reluctance model	proposed design	HWIPM (V_{nd}+V_{fe}/15)
HS rotor torque 3D (Nm)	15	1.62	14	12.9
PM volume in the inner rotor (mm^3)	109524	-	87619.2	74070
Total PM volume (V_{PM}) (mm^3)	204530	95030	182649.2	169100
Torque-to-inner rotor V_{PM} (Nm/mm^3)	0.000137	-	0.00016	0.00017
Torque-to-total V_{PM} (Nm/mm^3)	0.000073	0.000017	0.000074	0.000076
Maximum operating speed (rpm)	-	-	28943	12500

Furthermore, Fig. 28 presents a detailed analysis of deformation and stress distribution on the rotor under a nominal operating speed of 1000 rpm. The results indicate that the rotor maintains structural stability under these conditions, with deformation and stress levels remaining well within acceptable limits. This analysis underscores the proposed design's capability to withstand mechanical stress, making it reliable for both high-speed and high-torque applications.

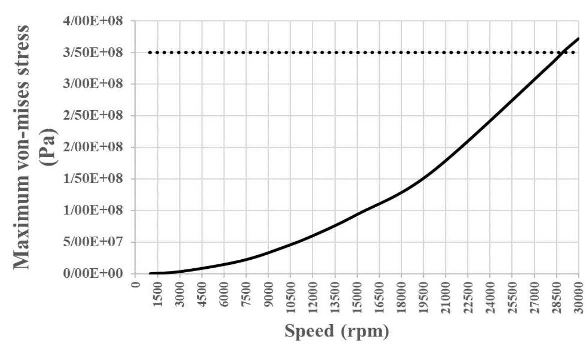

Fig 27. Maximum von Mises stress of the inner core based on the speed

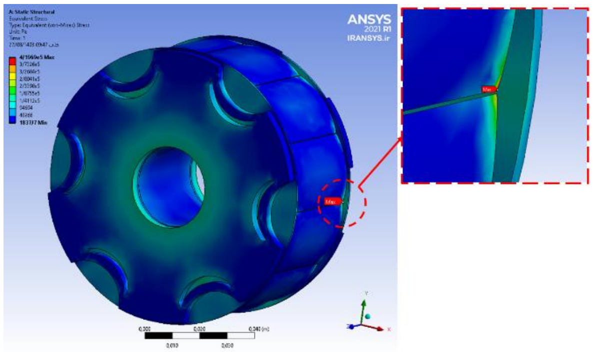

(a)

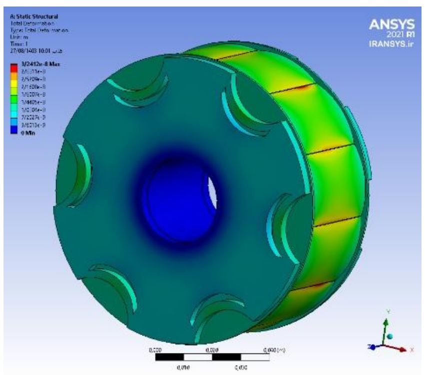

(b)

Fig 28. Mechanical analysis of inner rotor in 28500 rpm (a): Mises stress distribution and (b): total deformation distribution.

5 Conclusion

This study introduces a novel hybrid PM-reluctance structure for CMGs to address the challenges posed by the reliance on rare-earth magnets. By integrating reluctance and magnetic principles, the proposed design significantly reduces the volume of rare-earth magnets required, while maintaining high torque density and operational efficiency. Key innovations include a hybrid rotor structure with segmented reluctance and magnetic sections, optimized via PSO to enhance torque performance and minimize cogging torque. The results demonstrate a 20% reduction in magnet usage, with a 7% torque drop, coupled with a 23% improvement in the torque-to-volume ratio of the inner rotor magnets. Comparative analysis reveals that the proposed model outperforms fully magnetic and reluctance-based designs in terms of torque-to-magnet volume and torque-to-total magnet volume ratios. Additionally, the mechanical integrity of the design (validated through finite element analysis) ensures safe operation at high speeds up to 28943 rpm. This dual PM-reluctance model not only addresses critical material sustainability concerns but also provides an effective solution for high-performance CMGs, making it a compelling candidate for applications in high-speed, high-torque environments such as renewable energy systems and advanced industrial machinery.

Conflict of Interest

The authors declare no conflict of interest.

Declaration of generative AI and AI-assisted technologies

Statement sample: The authors declare that no generative AI or AI-assisted technologies were used in the writing process of this manuscript.

References

[1] H. Polinder, J. A. Ferreira, B. B. Jensen, A. B. Abrahamsen, K. Atallah and R. A. McMahon, "Trends in Wind Turbine Generator Systems," *IEEE Journal of Emerging and Selected Topics in Power Electronics*, vol. 1, no. 3, pp. 174-185, Sept. 2013.

[2] H. Polinder, J. A. Ferreira, B. B. Jensen, A. B. Abrahamsen, K. Atallah and R. A. McMahon, "Trends in Wind Turbine Generator Systems," *IEEE Journal of Emerging and Selected Topics in Power Electronics*, vol. 1, no. 3, pp. 174-185, Sept. 2013.

[3] L. Fang, D. Li and R. Qu, "Torque Improvement of Vernier Permanent Magnet Machine with Larger Rotor Pole Pairs Than Stator Teeth Number," *IEEE Transactions on Industrial Electronics*, vol. 70, no. 12, pp. 12648-12659, Dec. 2023.

[4] H. Baninajar, S. Modaresahmadi, H. Y. Wong, J. Bird, W. Williams and B. Dechant, "Designing a Halbach Rotor Magnetic Gear for a Marine Hydrokinetic Generator," *IEEE Transactions on Industry Applications*, vol. 58, no. 5, pp. 6069-6080, Sept.-Oct. 2022.

[5] J. J. Scheidler, V. M. Asnani and T. F. Tallerico, "NASA's Magnetic Gearing Research for Electrified Aircraft Propulsion," *2018 AIAA/IEEE Electric Aircraft Technologies Symposium (EATS)*, 2018, pp. 1-12.

[6] K. Atallah and D. Howe, “A novel high-performance magnetic gear,” *IEEE Transactions on Magnetics*, vol. 37, no. 4, pp. 2844–2846, Jul. 2001.

[7] M. Chen, K. T. Chau, W. Li, and C. Liu, “Cost-effectiveness comparison of coaxial magnetic gears with different magnet materials,” *IEEE Trans Magn*, vol. 50, no. 2, pp. 821–824, 2014.

[8] N. W. Frank and H. A. Toliyat, “Analysis of the concentric planetary magnetic gear with strengthened stator and interior permanent magnet inner rotor,” *IEEE Transactions on Industry Applications*, vol. 47, no. 4, pp. 1652–1660, Jul. 2011.

[9] F. Kucuk and S. Mousavi, “Development of a novel Coaxial Magnetic Gear,” *15th International Conference on Electrical Machines, Drives and Power Systems (ELMA)*, Jun. 2017, pp. 22–25.

[10] S. A. Afsari Kashani, “Rotor Pole Design of Radial Flux Magnetic Gear for Reduction of Flux Density Harmonics and Cogging Torque,” *IEEE Transactions on Applied Superconductivity*, vol. 29, no. 8, Dec. 2019.

[11] P. O. Rasmussen, T. O. Andersen, F. T. Jørgensen, and O. Nielsen, “Development of a high-performance magnetic gear,” *IEEE Transactions on Industry Applications*, vol. 41, no. 3, pp. 764–770, May 2005

[12] K. Li, S. Modaresahmadi, W. B. Williams, J. D. Wright, D. Som, and J. Z. Bird, “Designing and Experimentally Testing a Magnetic Gearbox for a Wind Turbine Demonstrator,” *IEEE Transactions on Industry Applications*, vol. 55, no. 4, pp. 3522–3533, Jul. 2019.

[13] K. Aiso, K. Akatsu, and Y. Aoyama, “A novel reluctance magnetic gear for high-speed motor,” *IEEE Transactions on Industry Applications*, vol. 55, no. 3, pp. 2690–2699, May 2019.

[14] S. Hasanpour, M. C. Gardner, M. Johnson, and H. A. Toliyat, “Comparison of Reluctance and Surface Permanent Magnet Coaxial Magnetic Gears,” *IEEE Energy Conversion Congress and Exposition*, *Institute of Electrical and Electronics Engineers Inc.*, Oct. 2020, pp. 307–314.

[15] S. A. Afsari Kashani, “Design and Optimization of Coaxial Reluctance Magnetic Gear with Different Rotor Topologies,” *IEEE Transactions on Industrial Electronics*, vol. 69, no. 1, pp. 101–109, Jan. 2022.

[16] R. Safarpour and S. Pakdelian, “Topology Optimization of the Reluctance Coaxial Magnetic Gear,” *IEEE Transactions on Magnetics*, vol. 58, no. 8, Aug. 2022.

[17] M. Amin Masoudi and S. A. Afsari, “The Optimal Design and an Analysis of a Hybrid W-Shaped IPM Rotor of Coaxial Magnetic Gear,” *IEEE Access*, vol. 12, pp. 81067–81074, 2024.

[18] M. M. Khaledi and S. A. A. Kashani, "Design of an L-Shaped Hybrid PM Array in Coaxial Magnetic Gear," *2025 16th Power Electronics, Drive Systems, and Technologies Conference (PEDSTC)*, Tabriz, Iran, Islamic Republic of, 2025, pp. 1-7.

[19] M. M. Khaledi and S. A. A. Kashani, "A New Hybrid Y-Type Rotor Topology for High-Performance Coaxial Magnetic Gear," *2024 4th International Conference on Electrical Machines and Drives (ICEMD)*, Tehran, Iran, Islamic Republic of, 2024, pp. 1-7.

[20] M. D. Nardo *et al.*, "Permanent Magnet Assisted Synchronous Reluctance Machine Design for Light Traction Applications," in *IEEE Transactions on Industry Applications*, vol. 60, no. 4, pp. 6079-6091, July-Aug. 2024.

[21] A. Nobahari, A. Vahedi and R. Nasiri-Zarandi, "A Modified Permanent Magnet-Assisted Synchronous Reluctance Motor Design for Torque Characteristics Improvement," in *IEEE Transactions on Energy Conversion*, vol. 37, no. 2, pp. 989-998, June 2022.

[22] J. Stander, “The specification of a small commercial wind energy conversion system for the South African Antarctic Research Base SANAE IV,” Jan. 2008.

[23] M. Muthusamy, J. Hendershot, and P. Pillay, “Design of a Spoke Type PMSM With SMC Stator Core for Traction Applications,” *Transactions on Industry Applications*, vol. 59, no. 2, pp. 1418–1436, Mar. 2023.

[24] S. E. M. Mohammadi, P. Chen, M. Moallem, B. Fahimi, and M. Kiani, “An Alternate Rotor Geometry for Switched Reluctance Machine with Reduced Torque Ripple,” *IEEE Transactions on Energy Conversion*, vol. 38, no. 2, pp. 939–947, Jun. 2023.

[25] Y. Tian, G. Liu, W. Zhao and J. Ji, "Design and Analysis of Coaxial Magnetic Gears Considering Rotor Losses," in *IEEE Transactions on Magnetics*, vol. 51, no. 11, pp. 1-4, Nov. 2015.

Biographies

MOSTAFA MADANCHI ZAJ was born in Kashan, Iran, in 2000. He received the B.S. degree in electrical engineering from University of Kashan, Kashan, Iran, in 2022. He received the M.Sc. degree in electrical engineering from University of Kashan, Kashan, Iran, in 2025. He is currently working as a research assistant in the modern electrical machine and magnetic materials laboratory, at University of Kashan. His research interests are magnetic gears, electrical machine design, and superconductors.

S. A. AFSARI was born in Kashan, IRAN, in 1994. He received B.S. degree in electrical engineering from K.N.Toosi University of Technology, Tehran, Iran, in 2007 and the M.Sc. degree from the University of Kashan, Kashan, Iran, in 2010, both in electrical power engineering, and the Ph.D. degree in Electrical Machine design from Iran University of Science and Technology (IUST), Tehran, Iran, in 2016. Following graduation, he joined University of Kashan, Kashan, Iran, as an assistant professor of the Electrical Power Group, and was also appointed as Director of the modern electrical machine and magnetic materials laboratory. His research interests are novel electrical machine design, magnetic gears, analytical methods, finite-element-method-based simulation techniques, optimization methods, and applied superconductors in power systems.